



ORIGINAL ARTICLE

Journal
of the American Ceramic Society

In-situ observation of AlN formation from Ni-Al solution using an electromagnetic levitation technique

Masayoshi Adachi¹ | Sonoko Hamaya¹ | Yuji Yamagata¹ | Andrew J. Loach² | Justin S. Fada³ | Laura G. Wilson² | Roger H. French² | Jennifer L. W. Carter² | Hiroyuki Fukuyama¹

¹Institute of Multidisciplinary Research for Advanced Materials (IMRAM), Tohoku University, Sendai, Japan

²Department of Materials Science and Engineering, Case Western Reserve University, Cleveland, OH, USA

³Department of Mechanical and Aerospace Engineering, Case Western Reserve University, Cleveland, OH, USA

Correspondence

Masayoshi Adachi and Hiroyuki Fukuyama, Institute of Multidisciplinary Research for Advanced Materials (IMRAM), Tohoku University, 2-1-1 Katahira, Sendai 980-8577, Japan.

Email: masayoshi.adachi.d7@tohoku.ac.jp (M. A.); hiroyuki.fukuyama.b6@tohoku.ac.jp (H. F.)

Funding information

Japan Society for the Promotion of Science, Grant/Award Number: JP26249113, JP26706013 and JP17K19067; National Science Foundation, Grant/Award Number: 1152716

Abstract

Aluminum nitride is a promising substrate material for AlGaN-based UV-LED. In order to develop a robust growth processing route for AlN single crystals, fundamental studies of solution growth experiments using Ni-Al alloy melts as a new solution system were performed. Al can be stably kept in solution the Ni-Al liquid even at high temperature; in addition, the driving force of the AlN formation reaction from solution can be controlled by solution composition and temperature. To investigate AlN crystal growth behavior we developed an in situ observation system using an electromagnetic levitation technique. AlN formation behavior, including nucleation and growth, was quantitatively analyzed by an image processing pipeline. The nucleation rate of AlN decreased with increasing growth temperature and decreasing aluminum composition. In addition, hexagonal c-axis oriented AlN crystal successfully grew on the levitated Ni-40 mol%Al droplet reacted at low driving force (1960 K), on the other hand, AlN crystal with dendritic morphology appeared on the sample with higher driving force (Ni-50 mol%Al, 1960 K). Thus, the nucleation rate and crystal morphology were dominated by the driving force of the AlN formation reaction.

KEYWORDS

aluminum nitride, crystal growth, nucleation, thermodynamics

1 | INTRODUCTION

Aluminum nitride (AlN) is a promising substrate material for AlGaN-based photonic and high-power devices such as deep ultraviolet light emitting diodes (UV-LED) and high-power electronic transistors. This is because AlN has a small lattice mismatch with AlGaN, high thermal conductivity, high UV transparency,^{1,2} and high dielectric breakdown strength.³ Therefore, the development of methodologies for mass production of single crystal AlN could transform an industry.

However, it is difficult to produce bulk AlN single crystals using melt solidification processes, such as the Czochralski method used for mass production of silicon, because AlN has a high dissociation pressure at high temperatures. Physical vapor transport (PVT) method,⁴⁻⁷ hydride vapor phase epitaxy (HVPE) method,⁸⁻¹⁰ and thermal nitridation of Al₂O₃¹¹ have been developed for AlN production. In the case of PVT method, growth of helical crystal has also been developed.^{12,13} However, fabricating larger diameter AlN bulk crystal at a reasonable cost has yet to be achieved.

This is an open access article under the terms of the Creative Commons Attribution License, which permits use, distribution and reproduction in any medium, provided the original work is properly cited.

© 2019 The Authors. *Journal of the American Ceramic Society* published by Wiley Periodicals, Inc. on behalf of American Ceramic Society (ACERS)

One of the promising methods of producing large diameter AlN single crystals is a solution growth method.^{14–16} In a solution growth method, the AlN crystal forms in liquid metals or alloys by controlling the degree of supersaturation of solute. Generally, high quality, defect free, crystal can be grown by a solution growth method because growth occurs at conditions close to thermal equilibrium. Recently, the authors have developed a solution growth method using Ga-Al solution.^{17–19} In this method, epitaxial AlN layer can be grown on nitrated sapphire substrate at 1573 K under normal pressure of nitrogen atmosphere. However, this Ga-Al solution method has not been used for industrial production of AlN because of its low growth rate.

The Ni-Al solution system is being explored in the present study because it could enable higher processing temperatures than Ga-Al solution which would increase the solution growth rate of AlN. In particular, Ni-rich compositions where the activity of Al in liquid Ni-Al alloy is kept low, $a \leq 10^{-2}$, as shown in Figure 1.²⁰ This keeps the Al stable in the liquid Ni-Al alloys even at high temperature. Moreover, it is possible to control the driving force of the AlN formation reaction in the Ni-Al solution by solution composition, nitrogen partial pressure, and temperature.

In situ observation of crystal growth is a powerful tool to understand the growth behavior and design an optimum crystal growth technique. Here, we have developed an in-situ observation system for solution growth of AlN crystal using an electromagnetic levitation (EML) in combination with an automated image processing pipeline²¹ to quantify nucleation and growth. The EML technique is generally used for the measurement of thermophysical properties^{22–27} or investigation of the solidification process^{28–30} of metallic melts. In this paper, we describe the details of the in-situ observation system and the quantitative analysis of the AlN nucleation and growth from the Ni-Al solution using computer vision

and materials data science methods.³¹ Moreover, the quality of the AlN crystal grown from the Ni-Al solution was subsequently characterized by scanning electron microscopy, X-ray diffractometry, and Raman spectroscopy.

2 | PRINCIPLE

Thermodynamics of the AlN formation in the Ni-Al solution is described below. AlN formation reaction is given as follows:



The equilibrium reaction constant (Equation 1) (K) is calculated from the activity of liquid aluminum (a_{Al}), activity of solid AlN (a_{AlN}) and equilibrium partial pressure of nitrogen gas ($p_{\text{N}_2}^{\text{eq}}$) as follows:

$$\ln K = \ln \frac{a_{\text{AlN}}^2}{a_{\text{Al}}^2 p_{\text{N}_2}^{\text{eq}}} = -2 \ln a_{\text{Al}} - \ln p_{\text{N}_2}^{\text{eq}} \quad (2)$$

Here, the standard states of a_{Al} and a_{AlN} are pure liquid Al and solid AlN, respectively, at standard pressure (1 bar), and partial pressure of nitrogen is standardized by 1 bar. The equilibrium reaction constant (K) is obtained from the standard Gibbs energy of formation of AlN reported by Nakao et al.³² The activity of liquid Al in the Ni-Al liquids are estimated using regular solution model based on the activity values at 1873 K reported by Desai et al.²⁰ Considering the equilibrium between Ni-Al solution and AlN under the current experimental condition, a_{AlN} is essentially unity. The driving force ($\Delta\mu$) of reaction (1) is the chemical affinity, which is defined as follows:

$$\begin{aligned} \Delta\mu &= 2\mu_{\text{Al}} + \mu_{\text{N}_2} - 2\mu_{\text{AlN}} \\ &= kT (\ln K + 2 \ln a_{\text{Al}} + \ln p_{\text{N}_2}) \\ &= kT (\ln p_{\text{N}_2} - \ln p_{\text{N}_2}^{\text{eq}}) \end{aligned} \quad (3)$$

Thus, the driving force is given by the difference between chemical potential of nitrogen gas at experimental and at equilibrium conditions. Equation (3) also indicates that the driving force is dominated by the equilibrium reaction constant (K), activity of Al in Ni-Al solution (a_{Al}), and experimental nitrogen partial pressure (p_{N_2}).

Figure 2 highlights the temperature dependence of the driving force of the AlN formation reaction for each composition of Ni-Al solution under 1 bar nitrogen partial pressure calculated from equation 3 utilizing the measured values of for activity of Al in Ni-Al reported by Desai²⁰ and standard Gibbs energy of formation of Al reported by Nakao.³² The driving force of AlN formation increases with decreasing

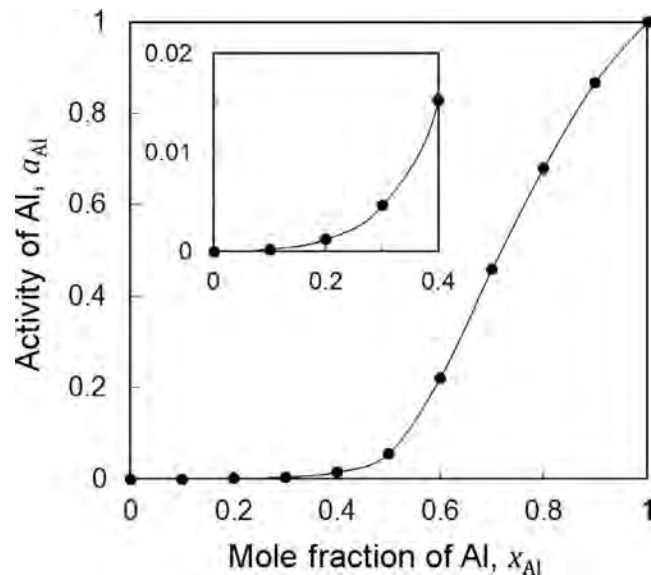


FIGURE 1 Composition dependence of activity of Al in liquid Ni-Al alloy at 1873 K²⁰

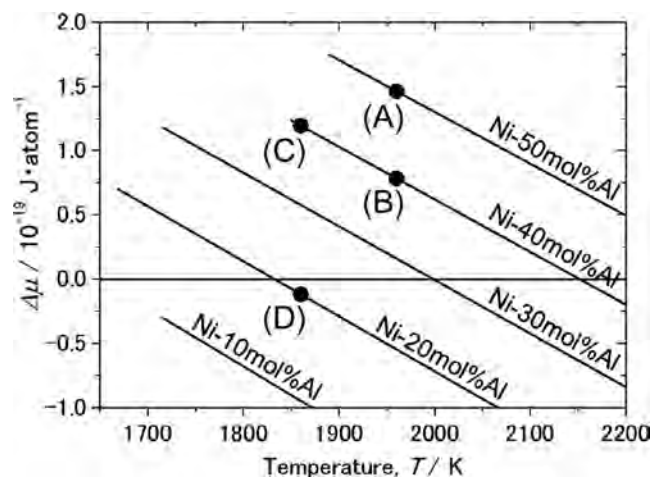


FIGURE 2 Temperature-dependent driving force of AlN formation on Ni-Al droplets for various compositions under 1 bar nitrogen partial pressure. The left-end of each line is the liquidus temperature for that alloy composition. The points (A-D) indicate that temperatures and compositions explored in this paper

temperature and with increasing Al concentration of the Ni-Al solution. AlN can be grown at the region of $\Delta\mu > 0$ as indicated by the horizontal line in Figure 2. Four experimental conditions (a-d) are presented in Figure 2: (a) Ni-50 mol%Al at 1960 K, (b) Ni-40 mol%Al at 1960 K, (c) Ni-40 mol%Al at 1860 K, and (d) Ni-20 mol%Al at 1860 K.

3 | EXPERIMENTAL PROCEDURE

3.1 | In situ observation of AlN formation

Spheres of Ni-Al alloy with compositions of Ni-20 mol%Al, Ni-40 mol%Al, and Ni-50 mol%Al were prepared by arc melting from pure Ni (99.99 mass%, Rare Metallic Co., Ltd.) and Al (99.99 mass%, The Nilaco Corporation). Diameter of the samples used for the AlN formation experiment was 6–8 mm.

Schematic of the experimental apparatus for in-situ observation of AlN growth is shown in Figure 3A. The sample was placed into an EML coil at the center of the chamber using a sintered boron nitride sample holder. The chamber was evacuated to 10^{-3} Pa by a turbo molecular pump and back filled with Ar-5 vol%H₂ (purity: 99.9999 vol%) and He (purity: 99.999 vol%) gases to atmospheric pressure. These gases were purified before entering the main chamber in a deoxidation column containing metallic Mg ribbon heated at 773 K as an oxygen getter. A radio-frequency power was applied to the levitation coil to levitate the sample. A static magnetic field generated by a superconducting magnet was also applied to the sample with strength of 4 T to maintain levitation stability. The static magnetic field suppresses surface oscillation and translational motion of the sample droplet as well as the convection flow in the

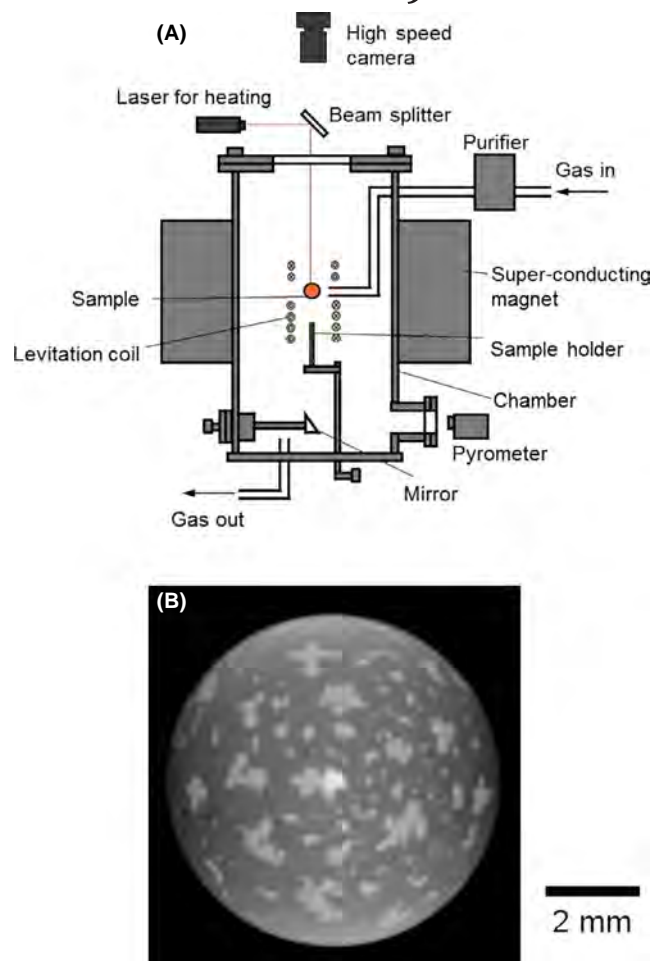


FIGURE 3 A, Experimental apparatus for in situ observation of AlN formation on the surface of Ni-Al droplet using EML. B, An image of the levitated droplet obtained by the high-speed camera

droplet.³³ Additionally, the static magnetic field results in the levitating droplet rotating about the vertical axis in Figure 3A parallel to the incident laser beam. After the sample is levitated by the radio frequency electromagnetic field, the sample temperature was controlled by laser irradiation (Jenoptik Japan Co., Ltd. DRV-S210-R, maximum output power: 210 W, wavelength: 807 nm). The sample temperature was monitored by a single-color pyrometer (LumaSense Technologies, IMPAC IGA140/MB25, 1.45–1.8 μ m). The pyrometer was calibrated with the liquidus temperature of each alloy, as indicated in Figure 2.²⁷ After the molten sample maintains stability, the purified nitrogen gas (Matheson Tri-Gas, Inc, Nanochem PuriFilter, PF-25) was introduced into the sample with a flow rate of 0.3 L/min. The introduction of the gas causes the formation of AlN to occur on the sample surface. Behavior of AlN formation was monitored by a high-speed camera (Mikrotron GmbH, MC1310) from top of the droplet at a frame rate of either 300 or 500 frames per second (fps). An image of the levitated droplet obtained by the high-speed camera is

shown in Figure 3B. The static magnetic field results in the droplet rotating about an axis parallel to the image plane normal. After AlN completely covered the sample surface, the levitated droplet was cooled and solidified by exposing the droplet to a flow of He gas. The solidified droplet was dropped on the sample holder by turning off the levitating magnetic field. As described later, the time required to cover the sample surface completely was different for each condition. The samples (a-d) were cooled by the He gas flow after 130 seconds, 390 seconds, 90 seconds and 1660 seconds from starting of nitrogen gas introducing, respectively.

3.2 | Image processing and analysis

The high-speed camera, above the spinning droplet (Figure 3), collects in situ observations of the AlN formation and produces a time-series of gray-scale images for each droplet studied, amounting to 300 000 individual images which were stored in a distributed computing cluster based on Hadoop and Hbase for efficient data handling.³⁴ These images are processed to extract useful metrics of the solidification process. Image processing was performed using Python (v2.7) libraries, including Numpy, Scipy, Matplotlib, Pandas, Seaborn, Skimage, OpenCV and Trackpy.^{35–37} The various steps of the image

processing are schematically presented in Figure 4. Using an automated image processing pipeline on the time series images, two metrics were extracted from each image in the video: the number of AlN nuclei visible and the area fraction of the surface where AlN crystallized. For both metrics, the surface area of the droplet analyzed excludes the area obscured by the laser spot. These metrics were combined with information about the video frame rates to quantify measures of the nucleation rate and the crystal growth rate.

Prior to extracting metrics from the images, the following pre-processing steps were applied: droplet centering, and adaptive equalization. The molten droplets are oscillating off-center slightly, and rotating around an axis perpendicular to the camera field of view in addition due to the applied static magnetic field.³³ The first step in the analysis was to center the droplet in the frame utilizing the median filter (numpy) and shifting (numpy.interpolation.shift) the center of the droplet to the center of the image array to remove the oscillating behavior. The rotation does not need to be removed for analysis but removal applying a constant counter rotation velocity is useful for visualization. Next, a denoising function (skimage.restoration.denoise_bilateral) was applied to remove spurious high/low intensity pixels. The droplet images exhibited a variable brightness that was consistent from frame to frame associated with variability in the lighting that was modeled as a sigmoid function. This functional

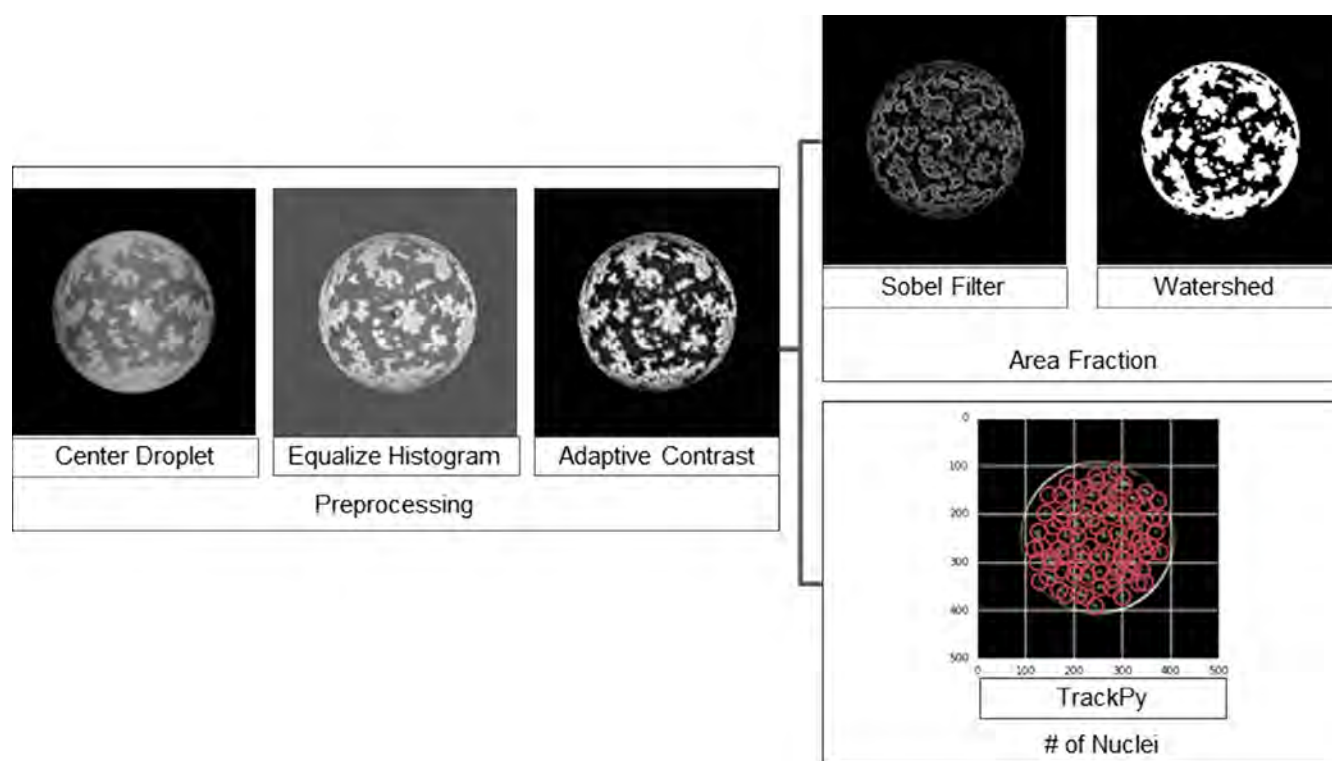


FIGURE 4 Schematic of the image processing procedures to quantify kinetic parameters of the formation of AlN on the levitated Ni-Al droplet

form defined an erosion mask to subtract the lighting in the molten droplet from subsequent images. Finally, the exposure function in the Skimage package was applied to maximize the image contrast while maintaining pixel rank order.

The surface coverage was calculated by following the general steps: preprocessing (ie, center the droplet, subtract an initial frame, adaptive equalization), edge finding with sobel filter, apply a watershed function, and finally calculation of metrics. A sobel filter³⁸ (skimage.filters library) was applied to find intensity gradients corresponding to the interface between AlN crystals and the Ni-Al liquid. Finally, a watershed function (skimage.segmentation.watershed) was applied to connect and fill in the pixels contained within the defined interface. The result at this stage of image processing was a black and white image showing the molten surface and background in black with the surface crystallization in white. The crystal growth rate was quantified as the area fraction of the molten droplet covered by crystals as a function of frame rate. Since the images are a 2D representation of a 3D surface, a stereological correction was applied using the conversion of the area of an annulus of a circle to the area of the zone of a sphere as a function of radial distance from the center of the circle:

$$\frac{A_{\text{zone}}}{A_{\text{annulus}}} = \frac{R \left(\sqrt{R^2 - (g - p/2)^2} - \sqrt{R^2 - (g + p/2)^2} \right)}{gp}, \quad (4)$$

where the radius of the sphere/circle, R (calculated from each frame), the distance from the center of the sphere (g), and the pixel width (p) all have self-consistent units. The total surface area of the droplet was calculated by segmenting the molten droplet from the black background. The area fraction of each area zone (defined by a pixel width) covered in crystals were calculated as the ratio of the number of pixels defined as crystals over the total number of pixels in the annulus of the droplet. This value was then weighted based on the stereological correction to output the fraction of the zone of the droplet, and summed together for the resulting percentage of coverage was then reported for each frame number.

The number of nuclei per image frame was calculated utilizing the trackpy function (trackpy) from the adaptive equalized images. The starting and ending frames to bound the nucleation event, were manually selected from the area fraction as a function of frame data, to include images associated with the first nucleation event. This package locates and annotates high contrast pixels. This defines the location of each nuclei on the surface of the droplet in each image frame.

3.3 | AlN characterization

Characterization of the AlN crystals was conducted on as-solidified droplets, with no surface pretreatment.

The surface morphology of the formed AlN crystals on the Ni-Al droplet surface was observed using a scanning electron microscopy with thermionic emission gun (JEOL Ltd., JCM-5700). Secondary electron images, using an acceleration voltage of 15 kV, were obtained in this study. Working distance was 10 mm.

X-ray diffraction, using an X-ray diffractometer (Bruker AXS GmbH, D8 discover μ MR, $\text{CuK}\alpha$), was conducted for phase identification and evaluation of crystal orientation. X-ray source assembly (Incoatec GmbH, I μ S) contained two multilayer mirrors for monochromatization was equipped, and a circular slit of 1 mm in diameter was used in the measurement. The XRD system was aligned to characterize the surface of the solidified droplet.

Raman spectroscopy (HORIBA Ltd., XploRA ONE) was conducted to confirm crystal orientation of the formed AlN crystal. Wavelength of incident laser was 532 nm. This was done to compare with Raman spectrum of AlN crystal in backscattering geometry with the laser beam incident on AlN (0002) surface, the peaks corresponding to E_2^H , E_2^L and A1(LO) mode reported by several researchers.^{39,40}

4 | RESULTS

4.1 | In situ observation of AlN growth on Ni-Al droplet

Figure 5A-D shows the top-view images of the AlN grown on the Ni-Al droplet surface during N_2 gas flowing observed by a high-speed camera under the respective growth conditions (a-d) as presented in Figure 2. The time zero for the time presented in Figure 5 was defined when AlN crystal formation began. The bright areas in Figure 5 are AlN crystals formed, except for the bright area in the center associated with the laser. Multiple nucleation events occurred simultaneously on the Ni-Al droplets. The surface of the levitated Ni-Al droplet was covered widely within a one second time-lapse in the case of Figure 5A and C; while the nucleation of AlN crystal took place more slowly in the case of Figure 5B and D. For samples (B) and (D), the nucleation occurred homogeneously at the initial stage as shown in Figure 5B and D at $t = 0.5$ s. After that, the nucleated AlN crystals gathered at the top of the droplet as shown in Figure 5B and D at $t = 2.0$ s. The levitated droplet rotates along vertical axis under the vertical static magnetic field. The density of liquid Ni-Al is larger than that of the AlN crystal formed on the droplet, which resulted in the AlN crystals gathered at the top of the droplet. Although the condition (d) is in a slightly negative $\Delta\mu$ region (as indicated in Figure 2), growth of AlN is observed. This could be due to the experimental uncertainty in the thermodynamic data used for calculation of Figure 2.

The number of nuclei of AlN crystals formed on the surface of levitated Ni-Al solutions as a function of time, obtained

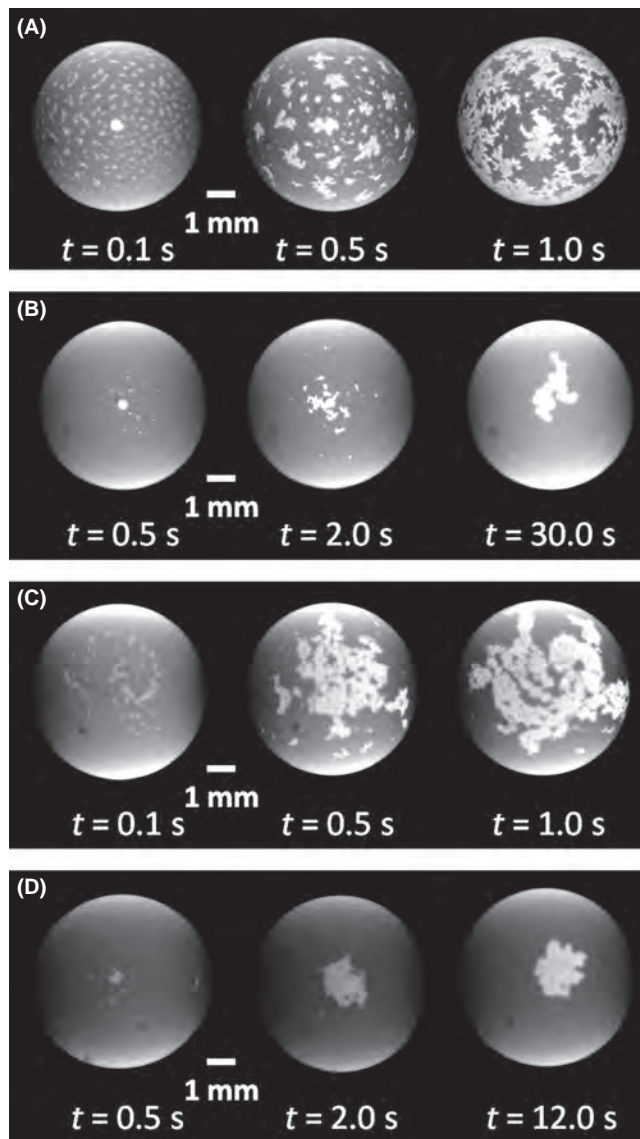


FIGURE 5 Top view images of the AlN grown on the Ni-Al droplet surface during N_2 gas flowing observed by high-speed camera under respective condition (A) Ni-50 mol%Al at 1960 K, (B) Ni-40 mol%Al at 1960 K, (C) Ni-40 mol%Al at 1860 K, (D) Ni-20 mol%Al at 1860 K. It should be noted that the timescale of the images varies

by the image processing, is presented in Figure 6. Here, the time zero was defined when nitrogen gas started to flow in the chamber. The number of nuclei initially increased before subsequently decreasing. Upon examination of the in-situ videos, this behavior can be attributed to the nucleated AlN crystals coalescing with each other. The initial nucleation rates for the samples (a) and (c) were faster than those for the samples (b) and (d). In addition, the incubation time before nucleation for the samples (b) and (d) were longer than others (a) and (c).

In the area fraction, the droplet is covered by AlN crystallized as a function of time, quantified from the image processing, is presented in Figure 7. The surface was rapidly covered with AlN crystals in the initial stage for the

samples (a) and (c), however, the growth rate slowed down followed by a second burst of growth activity. The reinvigorated growth in Figure 7 for conditions (A) and (C) corresponds with an increase in the number of nuclei observed in Figure 6. This indicated that the degree of supersaturation was exhausted on the droplet surface by the initial AlN crystal formation.

4.2 | Surface morphology of the formed AlN crystal

Figure 8 shows SEM images of the surface of the AlN crystals formed on the Ni-Al droplets after sample solidification. Dendritic AlN crystals were observed for the samples (a) and (c) indicative of an instability of the supersaturation on the droplet surface as observed in Figures 6 and 7. AlN crystals with hexagonal morphology were observed for the sample

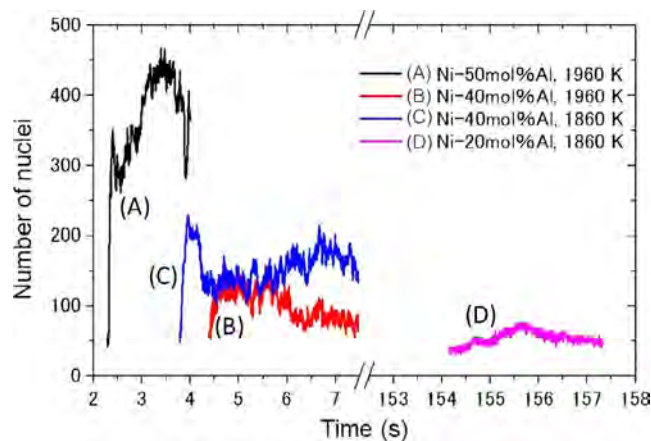


FIGURE 6 Time dependence of number of nuclei of AlN crystal formed on the surface of levitated Ni-Al droplets

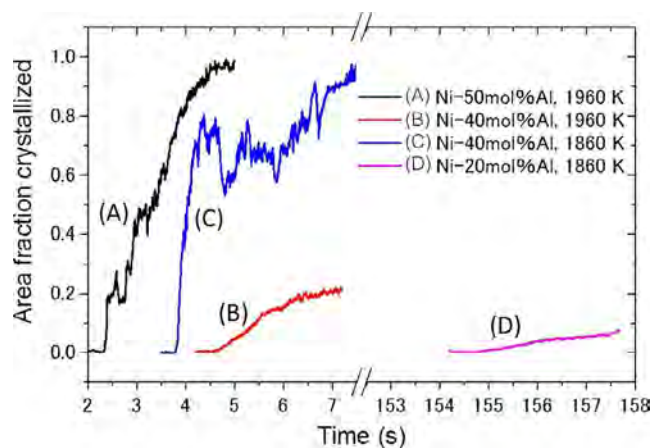
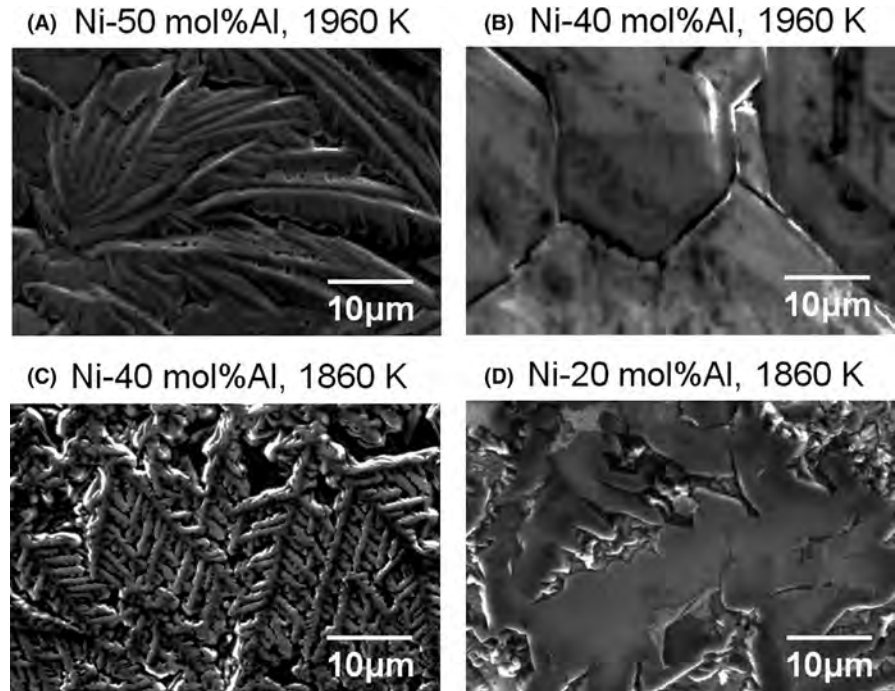


FIGURE 7 Time dependence of area fraction of AlN crystallized on the surface of the Ni-Al droplet

FIGURE 8 Surface morphologies of AlN crystal formed on the Ni-Al droplet observed by SEM. A, Ni-50 mol%Al at 1960 K, (B) Ni-40 mol%Al at 1960 K, (C) Ni-40 mol%Al at 1860 K, (D) Ni-20 mol%Al at 1860 K



(b), and facet planes were partially observed for the sample (d). The nucleation rate of the samples (b) and (d) were smaller compared with the other two samples as shown in Figure 6.

4.3 | Characterization of formed AlN crystals

As shown in Figure 8A and B, dendritic crystals were observed for the sample (a), on the other hand, hexagonal crystals were observed for the sample (b). For comparison, these AlN crystals formed at (a) Ni-50 mol%Al at 1960 K, (b) Ni-40 mol%Al at 1960 K were characterized by X-ray diffractometry. Figure 9 shows XRD 2θ - ω profiles for surfaces of samples (a) and (b). As can be seen, polycrystalline AlN was formed for the sample (a) as indicated by the presence of many XRD peaks. On the other hand, only a AlN (0002) peak is observed in the 2θ - ω profile for the sample (b), indicating that a single c-axis oriented AlN crystal successfully grew within the field of view of the XRD source. Also, shown in the XRD spectra of sample (b) in Figure 9 is a NiAl peak, which could be an indication of the AlN film thickness.

Figure 10 shows the Raman spectrum of the AlN crystal for the sample (b) in backscattering geometry with the laser beam incident on the normal direction to the surface. The peak corresponding to E_2^H mode in Figure 10 appeared at 674 cm^{-1} . On the other hand, phonon frequency of unstrained AlN was reported as 657 cm^{-1} .⁴⁰ Yang et al have investigated relationship between residual stress and Raman shift corresponding to E_2^H mode of AlN film.⁴¹ According to

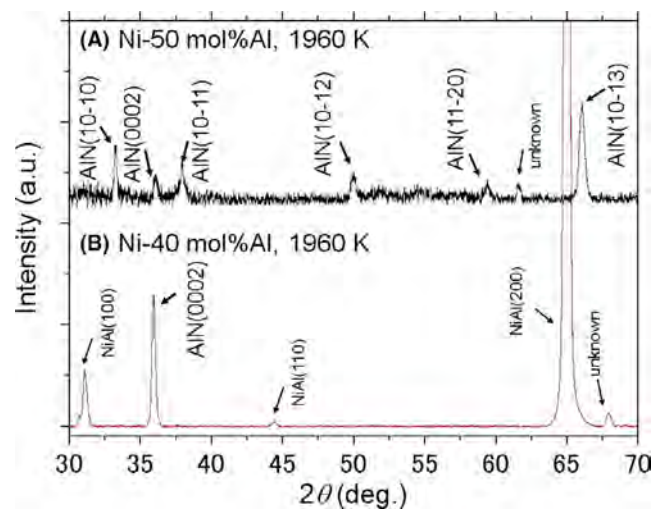


FIGURE 9 XRD 2θ - ω profiles of AlN formed at 1960 K on Ni-50 mol%Al and Ni-40 mol%Al. The distribution of peaks in the Ni-50 mol%Al sample (A) is consistent with a fine-grain film, while the peaks in the Ni-40 mol%Al sample (B) is consistent with a single crystal larger than the X-ray spot size

the literature,⁴¹ peak shift to higher wavenumbers indicates that compressive stress exist in the c-plane AlN film. In our experiment, the levitated Ni-Al droplet was cooled and solidified by exposing the droplet to flowing He gas after AlN formation. The radially compressive stress could be generated during the cooling process due to the mismatch between the thermal expansion coefficients of AlN and the Ni-Al alloy. However, AlN can grow without any interfacial stress during the nitridation process because AlN crystal formed on the liquid state Ni-Al solution.

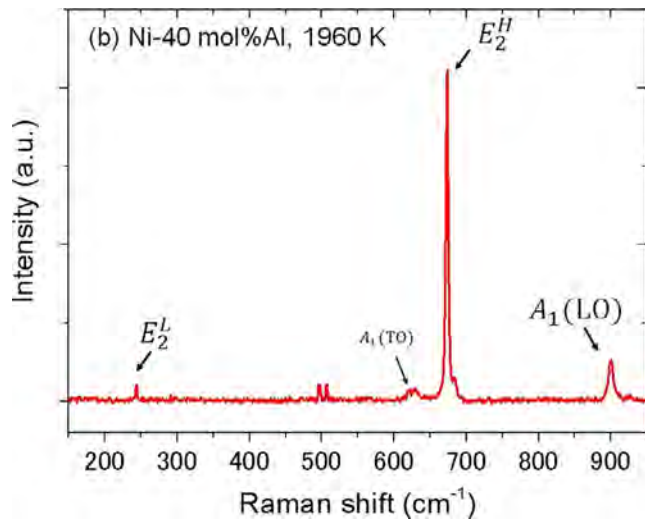


FIGURE 10 Raman Spectrum of AlN formed on Ni-40 mol%Al at 1960 K

5 | DISCUSSION

According to classical nucleation theory, the change in Gibbs energy homogeneous formation of a nucleus with critical size r^* is given by Ref. ⁴²:

$$\Delta G^* = \frac{16\pi\sigma^3 v^2}{3\Delta\mu^2}. \quad (5)$$

Here, σ , v , $\Delta\mu$ are the surface energy of the nucleus, the volume per formula unit of AlN, and the driving force per formula unit of the AlN formation, respectively. The nucleation rate J is expressed with a constant C as

$$J = C \exp\left(-\frac{\Delta U}{kT}\right) \exp\left(-\frac{\Delta G^*}{kT}\right). \quad (6)$$

Here, ΔU is the desolvation energy between the solute and the solvent.⁴² The atoms of the Al should break the bonds with the atoms of Ni before being attached to the nucleus. As shown in Figure 6, the initial nucleation rate of sample (c) was higher than sample (b). It indicates that the driving force of the AlN formation reaction ($\Delta\mu$) dominates the initial nucleation rate under these growth conditions. Also, for other samples, the driving forces of AlN formation reaction for the samples (a) and (c) were larger compared to with the samples (b) and (d). Therefore, the nucleation rates for the samples (a) and (c) were higher compared with the samples (b) and (d) as shown in Figure 5.

The driving force ($\Delta\mu$) also affects crystal morphology. As shown in Figure 8A, dendritic polycrystalline AlN grew for the sample. On the other hand, hexagonal c-plane AlN grew under the growth condition that had lower $\Delta\mu$ condition compared with the sample (a) as shown in

Figure 8B. In the case of high growth rate, a gradient in the degree of local supersaturation (the local supersaturation degree gradient) existed around the nucleated AlN crystal. The supersaturation degree gradient caused the dendritic AlN growth. On the other hand, in the case of low growth rate, the AlN grew slowly with lower growth rate of c-plane AlN compared with a- and m-planes AlN, which resulted in large hexagonal c-plane AlN grains appeared on the surface. For the sample (a), the droplet surface was completely covered with the AlN in a short time as shown in Figure 7, therefore, there was not enough time to grow large grains of AlN compared with sample (b). In addition, temperature also affects crystal morphology. From the comparison between Figure 8A and 8, typical dendrite shape appeared on the sample (c), despite similar $\Delta\mu$. It was considered that this variation was caused by the difference in diffusion in the solution.

6 | SUMMARY

In order to develop a novel solution growth method for the AlN crystal, fundamental studies on the AlN growth using the Ni-Al solution were conducted. The driving force of the AlN formation reaction in the Ni-Al solution was controlled by solution composition and growth temperature. To investigate the crystal growth behavior, we developed an in situ observation system using electromagnetic levitation. The nucleation rate of AlN decreased with increasing reaction temperature and decreasing of Al composition in the solution. The decrease in the Al composition results in a decrease in the driving force of AlN formation that controls the susceptibility of the nucleated structures to grow with the stable planer growth. Hexagonal c-axis-oriented AlN crystal successfully grew on the liquid Ni-40 mol%Al droplet at 1960 K, on the other hand, polycrystalline AlN with dendritic morphology appeared on the sample with higher driving forces or lower temperature. Thus, the nucleation rate and crystal morphology were dominated by the driving force of the AlN formation reaction.

ACKNOWLEDGMENTS

This work was supported by JSPS KAKENHI Grant Number JP26706013, JP17K19067 and JP26249113. The work conducted by the CWRU researchers L. G. Wilson and J. L. W. Carter on the image processing pipeline was funded by the National Science Foundation under Grant No. 1152716. The authors acknowledge the assistance of B. G. Pierce and A. M. Karimi in the image processing. This materials data science collaboration between Tohoku University and Case Western Reserve University was fostered under the Japanese MEXT Top Global program.

CONFLICT OF INTEREST

The authors declare no conflict of interest.

ORCID

Masayoshi Adachi  <https://orcid.org/0000-0002-8848-4681>

Justin S. Fada  <https://orcid.org/0000-0002-0029-5051>

Roger H. French  <https://orcid.org/0000-0002-6162-0532>

Jennifer L. W. Carter  <https://orcid.org/0000-0001-6702-729X>

Hiroyuki Fukuyama  <https://orcid.org/0000-0003-0753-4403>

REFERENCES

- Jones DJ, French RH, Mülleijans H, Loughin S, Dorneich AD, Garcia PF. Optical properties of AlN determined by vacuum ultraviolet spectroscopy and spectroscopic ellipsometry data. *J Mater Res*. 1999;14:4337–44.
- Loughin S, French RH. Aluminum nitride (AlN). In: Palik ED editor. *Handbook of optical constants of solids*, Vol. 3. USA: Academic Press; 1998; p. 373–401.
- Morkoc H. *Nitride semiconductor devices*, 1st edn. Weinheim: Wiley-VCH, 2013.
- Mueller SG, Bondokov RT, Morgan KE, Slack GA, Schujman SB, Grandusky J, et al. The progress of AlN bulk growth and epitaxy for electronic applications. *Phys Stat Sol A*. 2009;206:1153–9.
- Langhans F, Kiefer S, Hartmann C, Markurt T, Schulz T, Guguschev C, et al. Precipitates originating from tungsten crucible parts in AlN bulk crystals grown by the PVT method. *Cryst Res Technol*. 2016;51:129–36.
- Dalmau R, Craft HS, Britt J, Paisley E, Moody B, Guo JQ, et al. High quality AlN single crystal substrates for AlGaN-based devices. *Mater Sci Forum*. 2018;924:923–6.
- Jin L, Zhang H, Han J, Zhao CL, Yao T, Song B. Control of AlN single crystal nucleation: An insight into the crystal growth habit in the initial stages of the physical vapor transport. *Mater Express*. 2015;5:129–36.
- Soukhoveev V, Kovalenkov O, Ivantsov A, Syrkin A, Usikov A, Maslennikov V, et al. Recent results on AlN growth by HVPE and fabrication of free standing AlN wafers. *Phys Stat Sol C*. 2006;3:1653–7.
- Kumagai Y, Kubota K, Nagashima T, Kinoshita T, Dalmau R, Schlessner R, et al. Preparation of a freestanding AlN substrate from a thick AlN layer grown by hydride vapor phase epitaxy on a bulk AlN substrate prepared by physical vapor transport. *Appl Phys Express*. 2012;5:055504-1–3.
- Tojo S, Yamamoto R, Tanaka R, Thieu QT, Togashi R, Nagashima T, et al. Influence of high-temperature processing on the surface properties of bulk AlN substrates. *J Cryst Growth*. 2016;446:33–8.
- Fukuyama H, Kato M, You Y, Ohtsuka M. Growth mechanism of AlN crystals via thermal nitridation of sintered $\text{Al}_2\text{O}_3\text{-ZrO}_2$ plates. *Ceram Int*. 2016;42:5153–9.
- Zhang XH, Shao RW, Jin L, Wang JY, Zheng K, Zhao CL, et al. Helical growth of aluminum nitride: new insights into its growth habit from nanostructures to single crystals. *Sci Rep*. 2015;5:10087-1–12.
- Jin L, Zhang H, Pan R, Xu P, Han J, Zhang X, et al. Observation of the long afterglow in AlN helices. *Nano Lett*. 2015;15:6575–81.
- Kamei K, Shirai Y, Tanaka T, Okada N, Yauchi A, Amano H. Solution growth of AlN single crystal using Cu solvent under atmospheric pressure nitrogen. *Phys Stat Sol C*. 2007;4:2211–4.
- Isobe H, Kawamura F, Kawahara M, Yoshimura M, Mori Y, Sasaki T. Synthesis of AlN grains and liquid-phase-epitaxy (LPE) growth of AlN films using Sn-Ca mixed flux. *Jpn J Appl Phys*. 2005;44:L488–L490.
- Kangawa Y, Toki R, Yayama T, Epelbaum BM, Novel KK. Solution growth method of bulk AlN using Al and Li_3N solid sources. *Appl Phys Express*. 2011;4:095501-1–3.
- Adachi M, Maeda K, Tanaka A, Kobatake H, Fukuyama H. Homoepitaxial growth of AlN on nitrided sapphire by LPE method using Ga–Al binary solution. *Phys Stat Sol A*. 2011;208:1494–7.
- Adachi M, Tsuda K, Sugiyama M, Iida J, Tanaka A, Fukuyama H. High-quality AlN layer homoepitaxially grown on nitrided a-plane sapphire using a Ga–Al flux. *Appl Phys Express*. 2013;6:091101-1–3.
- Adachi M, Takasugi M, Sugiyama M, Iida J, Tanaka A, Fukuyama H. Polarity inversion and growth mechanism of AlN layer grown on nitrided sapphire substrate using Ga–Al liquid-phase epitaxy. *Phys Stat Soli B*. 2015;252:743–7.
- Desai PD. Thermodynamic properties of selected binary aluminum alloy systems. *J Phys Chem Ref data*. 1987;16:109–24.
- Karimi AM, Fada JS, Hossain MA, Yang S, Peshek TJ, Braid JL, et al. Automated pipeline for photovoltaic module electroluminescence image processing and degradation feature classification. *IEEE J Photovolt*. 2019;9:1324–35.
- Fukuyama H, Kobatake H, Takahashi K, Minato I, Tsukada T, Awaji S. Development of modulated laser calorimetry using a solid platinum sphere as a reference. *Meas Sci Technol*. 2007;18:2059–66.
- Kobatake H, Fukuyama H, Minato I, Tsukada T, Awaji S. Noncontact modulated laser calorimetry of liquid silicon in a static magnetic field. *J Appl Phys*. 2008;104:054901-1–8.
- Kobatake H, Khosroabadi H, Fukuyama H. Normal spectral emissivity measurement of liquid iron and nickel using electromagnetic levitation in direct current magnetic field. *Metall Mater Trans A*. 2012;43:2466–72.
- Watanabe M, Adachi M, Fukuyama H. Densities of Fe–Ni melts and thermodynamic correlations. *J Mater Sci*. 2016;51:3303–10.
- Watanabe M, Takano J, Adachi M, Uchikoshi M, Fukuyama H. Thermophysical properties of liquid Co measured by electromagnetic levitation technique in a static magnetic field. *J Chem Thermodynamics*. 2018;121:145–52.
- Adachi M, Sato A, Hamaya S, Ohtsuka M, Fukuyama H. Containerless measurements of the liquid-state density of Ni–Al alloys for use as turbine blade materials. *SN Appl Sci*. 2019;1:18-1-7.
- Herlach DM. Non-equilibrium solidification of undercooled metallic melts. *Mater Sci Eng R*. 1994;12:177–272.
- Nagashio K, Adachi M, Higuchi K, Mizuno A, Watanabe M, Kuribayashi K, et al. Real-time x-ray observation of solidification from undercooled Si melt. *J Appl Phys*. 2006;100:033524-1–6.
- Li M, Nagashio K, Ishikawa T, Mizuno A, Adachi M, Watanabe M, et al. Microstructure formation and in situ phase identification from undercooled Co–61.8 at.% Si melts solidified on an electromagnetic levitator and an electrostatic levitator. *Acta Mater*. 2008;56:2514–25.

31. Guire ED, Bartolo L, Brindle R, Devanathan R, Dickey EC, Fessler J, et al. Data-driven glass/ceramic science research: Insights from the glass and ceramic and data science/informatics communities. *J Am Ceram Soc.* 2019;102:6385–406.
32. Nakao W, Fukuyama H, Nagata K. Gibbs energy change of carbothermal nitridation reaction of Al_2O_3 to form AlN and reassessment of thermochemical properties of AlN. *J Am Ceram Soc.* 2002;85:889–96.
33. Yasuda H, Ohnaka I, Ninomiya Y, Ishii R, Fujita S, Kishio K, et al. Levitation of metallic melt by using the simultaneous imposition of the alternating and the static magnetic fields. *J Cryst Growth.* 2004;260:475–85.
34. Hu Y, Gunapati VY, Zhao P, Gordon D, Wheeler NR, Hossain M, et al. A nonrelational data warehouse for the analysis of field and laboratory data from multiple heterogeneous photovoltaic test sites. *IEEE J Photovolt.* 2017;7:230–6.
35. Python Software Foundation: Python 2.7.16. [homepage on the Internet]. 2019 [updated 2019 Jul 11; cited 2019 Jul 23]. Available from: <https://docs.python.org/2.7/>.
36. Jones E, Oliphant T, Peterson P. SciPy: open source scientific tools for Python. 2001. Available from: <http://www.scipy.org/>.
37. Bradski G. The OpenCV Library: Dr. Dobb's Journal of Software Tools. 2000. Available from: <https://opencv.org/>.
38. Russ JC. The image processing handbook, 4th edn. Boca Raton FL: CRC Press, 2002.
39. McNeil LE, Grimsditch M, French RH. Vibrational spectroscopy of aluminum nitride. *J Am Ceram Soc.* 1993;76:1132–6.
40. Kuball M. Raman spectroscopy of GaN, AlGaIn and AlN for process and growth monitoring/control. *Surf Interface Anal.* 2001;31:987–99.
41. Yang S, Miyagawa R, Miyake H, Hiramatsu K, Harima H. Raman scattering spectroscopy of residual stresses in epitaxial AlN films. *Appl Phys Express.* 2011;4:031001-1–3.
42. Markov IV. Crystal growth for beginners, 2nd edn. Singapore: World Scientific Publishing, 2003.

How to cite this article: Adachi M, Hamaya S, Yamagata Y, et al. In-situ observation of AlN formation from Ni-Al solution using an electromagnetic levitation technique. *J Am Ceram Soc.* 2019;00:1–10. <https://doi.org/10.1111/jace.16960>